

# Inverting Adversarially Robust Networks for Image Synthesis

Renan A. Rojas-Gomez   Raymond A. Yeh   Minh N. Do  
University of Illinois at Urbana-Champaign  
{renanar2,yeh17,minhdo}@illinois.edu

Anh Nguyen  
Auburn University  
anh.ng8@gmail.com

## Abstract

Despite unconditional feature inverters being the foundation of many synthesis tasks [32, 43, 46, 53], training them requires a large computational overhead [12], decoding capacity [10] or additional autoregressive priors [17]. We propose to train an adversarially robust encoder [34] to learn disentangled and perceptually-aligned bottleneck features, making them easily invertible. Then, by training a simple generator with the mirror architecture of the encoder, we achieve superior reconstructions and generalization over standard approaches [12]. We exploit such properties using an encoding-decoding network based on AR features and demonstrate its outstanding performance on three applications: anomaly detection, style transfer and image denoising. Comparisons against alternative learn-based methods show that our model attains improved performance with significantly less training parameters.<sup>1</sup>

## 1. Introduction

Deep classifiers trained on large-scale datasets extract meaningful high-level features of natural images, making them an essential tool for manipulation tasks such as style transfer [32], image inpainting [41] and composition [53], among others. State-of-the-art manipulation techniques use a decoder or *image generator* to map high-level features to natural images. Extensive work has explored how to learn such a map, leading to encoding-decoding models with photorealistic results [21]. Interestingly, the generator itself enables impressive synthesis use cases, *e.g.* anomaly detection [20] and visualizing neural networks [42, 43, 46].

Inverting such representations requires the generator to be considerably more complex than the encoder [10, 12, 13, 41], drastically increasing its computational demand. This is explained by the fact that the encoder bottleneck learns entangled features that are harder to invert [10]. To surpass this challenge, we propose to train the generator with disentangled, perceptually-aligned bottleneck representations.

<sup>1</sup>Code and models available at [https://github.com/renanrojasg/adv\\_robust\\_autoencoder](https://github.com/renanrojasg/adv_robust_autoencoder)

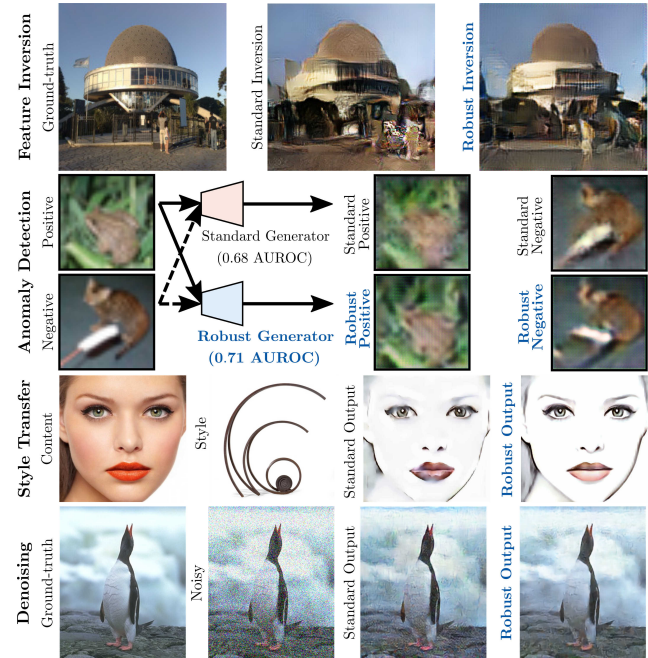


Figure 1. By learning a map from the adversarially robust (AR) feature space to the pixel domain, our autoencoder attains superior performance over standard models on various tasks including feature inversion, anomaly detection, style transfer, and denoising. Our AR autoencoder not only outperforms standard ones using less trainable parameters, but also generalizes to reconstructing images at unseen resolutions without retraining (Figs. 4–5).

Similarly to work on feature inversion and Plug-and-Play Generative Nets [12, 41], we adopt a pre-trained classifier as encoder and train an image generator to invert its contracted representations, yielding an autoencoder for real data. However, instead of using feature extractors trained on natural images, we propose to train the encoder on adversarial examples [34]. This fundamental difference equips our *adversarially robust (AR) autoencoder* with disentangled representations that are perceptually-aligned with human vision [16, 52], resulting in favorable inversion properties (Fig. 1).

To the best of our knowledge, we are the first approach to train an autoencoder on both adversarial and real images. To highlight the properties of our AR autoencoder’s bottleneck features and their effectiveness, we adopt a generator

corresponding to the *mirror* architecture of the encoder, *i.e.* without additional decoding layers [10, 53] or additional autoregressive networks [17, 47]. Our main findings are:

- Training a generator on AR features largely improves the reconstruction over standard approaches. Experiments with AlexNet [31] and VGG-16 [55] on ImageNet [50], and ResNet [24] on CIFAR-10 [30] reveal that the accuracy gain obtained by our AR autoencoder generalizes to different model complexities and robust training schemes (Sec. 4.1).
- Our AR autoencoder is remarkably robust to scale changes, as shown on upscaled ImageNet samples and high-resolution images (Fig. 4). Experiments on DIV2K [1] show it accurately reconstructs high-resolution images without finetuning, despite being trained on low-resolution images (Sec. 4.3).
- Comparisons against state-of-the-art inversion methods show that our generator substantially outperforms iterative optimization techniques [16] in terms of PSNR, SSIM, and LPIPS [63]. It also attains comparable accuracy to the well-established DeepSiM model [11] with a much lower model complexity (Sec. 4.4).
- Based on these properties, we exploit our model in three downstream tasks: anomaly detection [20], universal style transfer [32] and image denoising [41]. Detailed comparisons against recent methods show our model largely improves over standard approaches, attaining state-of-the-art performance (Sec. 5).

## 2. Preliminaries

Our model exploits meaningful representations to reconstruct high-quality images, which is related to the celebrated feature inversion framework. Specifically, we explore AR features as a strong prior to obtain photorealism. For a clear understanding of our proposal, we review the fundamental concepts of feature inversion and AR training.

**Feature Inversion.** Consider a target image  $x_0 \in \mathbb{R}^{W \times H \times C}$  and its contracted representation  $f_0 \triangleq F_\theta(x_0) \in \mathbb{R}^{W' \times H' \times C'}$ , where  $F_\theta$  denotes the target model, *e.g.* AlexNet, with parameters  $\theta \in \mathbb{R}^T$  and  $W'H'C' \ll WHC$ . Features extracted by  $F_\theta$  encapsulate rich input information that can either be used for the task it was trained on or transferred [44] to a related domain and used for applications such as image enhancement and manipulation [19, 27].

An effective way to leverage these representations is by training a second model, a feature inverter, to map them to the pixel domain. This way, deep features can be manipulated and transformed into images [11, 12]. Also, since deep features preserve partial input information, inverting them elucidates what kind of attributes they encode. Based

on these, *feature inversion* [11, 35, 54] has been extensively studied for visualization and understanding purposes as well as for synthesis and manipulation tasks. Typically, feature inversion is formulated as an optimization problem:

$$\hat{x} = \underset{x \in \mathbb{R}^{W \times H \times C}}{\operatorname{argmin}} \mathcal{F}(F_\theta(x), f_0) + \lambda \mathcal{R}(x), \quad (1)$$

where  $\hat{x}$  is the estimated image,  $\mathcal{F}(F_\theta(x), f_0)$  the fidelity term between estimated and target representations,  $F_\theta(x)$  and  $f_0$  respectively.  $\mathcal{R}(x)$  denotes the regularization term imposing *a priori* constraints in the pixel domain and  $\lambda \in \mathbb{R}_{++}$  balances between fidelity and regularization terms.

**Adversarial Robustness.** Adversarial training adds perturbations to the input data and lets the network learn how to classify in the presence of such adversarial attacks [3, 22, 34]. Consider the image classification task with annotated dataset  $\mathcal{K}$ . Let an annotated pair correspond to image  $x \in \mathbb{R}^{W \times H \times C}$  and its one-hot encoded label  $y \in \{0, 1\}^{|\mathcal{C}|}$ , where  $\mathcal{C}$  is the set of possible classes. From the definition by Madry *et al.* [34], a perturbed input is denoted by  $x' = x + \delta$ , where  $x'$  is the perturbed sample and  $\delta$  the perturbation. Let the set of perturbations be bounded by the  $\ell_p$  ball for  $p \in \{2, \infty\}$ ,  $\mathcal{S} : \{\delta, \|\delta\|_p \leq \varepsilon\}$ . Then, the AR training corresponds to an optimization problem:

$$\tilde{\theta} = \arg \min_{\theta} \mathbb{E}_{(x,y) \sim \mathcal{K}} \left[ \max_{\delta \in \mathcal{S}} \mathcal{L}_{x',y}(\theta) \right], \quad (2)$$

where  $\tilde{\theta} \in \mathbb{R}^T$  are optimal classifier weights and  $\mathcal{L}_{x',y}(\theta)$  the negative log-likelihood. The goal is to minimize  $\mathcal{L}_{x',y}(\theta)$  in the presence of the worst possible adversary.

## 3. Proposed Method

### 3.1. Adversarially Robust Encoder-Decoder

We propose an autoencoder architecture (Fig. 2a) to extract bottleneck AR features of arbitrary input images, manipulate them for a given synthesis or enhancement task, and map the results back to images. We denote the AR feature extractor as  $F_{\tilde{\theta}}$ , where  $\tilde{\theta}$  are the AR model weights (Sec. 2). Robust features are transformed into images using a CNN-based generator denoted as  $G_{\tilde{\phi}}$  with  $\tilde{\phi}$  being the generator's weights learned by inverting AR features.

Primarily, we use AlexNet [31] (common in inversion work [12, 57]) to extract AR features from its conv5 layer, providing a good tradeoff between dimensionality reduction and data preservation [12]. Additionally, we explore more complex AR encoders from the VGG and ResNet families and evaluate their improvement over standard versions (See Sec. A3.1 for architecture and training details).

### 3.2. Image Decoder: Optimization Criteria

Our model is trained via the DeePSiM framework [12] with modified optimality criteria. Given a pre-trained AR

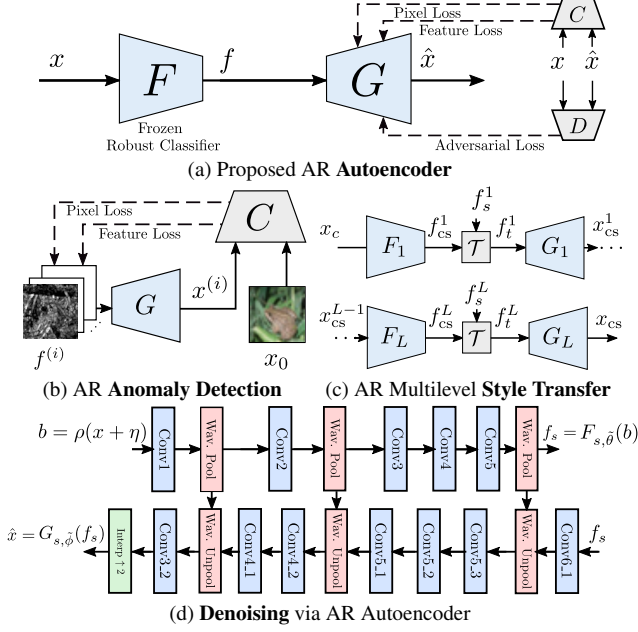


Figure 2. Image Synthesis Tasks using AR representations.

encoder  $F_{\tilde{\theta}}$ , the generator  $G_{\tilde{\phi}}$  is trained using  $\ell_1$  per-pixel,  $\ell_2$  feature and GAN losses, where the feature loss aligns AR features, known to be *perceptually aligned* [16].

Let  $\hat{x} = G_{\tilde{\phi}}(f)$  denote the reconstruction of image  $x$ , where  $f = F_{\tilde{\theta}}(x)$  are its AR features. Our framework uses two additional modules: A discriminator and a high-level feature extractor. The discriminator  $D_{\psi} : \mathbb{R}^{W \times H \times C} \mapsto [0, 1]$ , where  $\psi$  are the model parameters, predicts the probability of an image being real. The feature extractor obtains deep representations of a reconstructed image to compare them against those of the target image, e.g. we compare the same AlexNet conv5 AR features used for encoding. Thus, the feature extractor is equivalent to the AR encoder  $F_{\tilde{\theta}}$ . Considering fixed parameters  $\tilde{\theta}$  and an image dataset  $\tilde{\mathcal{K}}$ , the optimal generator parameters correspond to:

$$\tilde{\phi} = \arg \min_{\phi} \lambda_{\text{pix}} \mathcal{L}_{\text{pix}}(\phi) + \lambda_{\text{feat}} \mathcal{L}_{\text{feat}}(\phi, \tilde{\theta}) \quad (3)$$

$$+ \lambda_{\text{adv}} \mathcal{L}_{\text{adv}}(\phi, \psi),$$

$$\mathcal{L}_{\text{pix}}(\phi) \triangleq \mathbb{E}_{x \sim \tilde{\mathcal{K}}} \|x - \mathcal{G}_{\phi}(f)\|_1, \quad (4)$$

$$\mathcal{L}_{\text{feat}}(\phi, \tilde{\theta}) \triangleq \mathbb{E}_{x \sim \tilde{\mathcal{K}}} \|f - F_{\tilde{\theta}} \circ \mathcal{G}_{\phi}(f)\|_2^2, \quad (5)$$

$$\mathcal{L}_{\text{adv}}(\phi, \psi) \triangleq \mathbb{E}_{x \sim \tilde{\mathcal{K}}} [-\log D_{\psi} \circ \mathcal{G}_{\phi}(f)], \quad (6)$$

where  $\lambda_{\text{pix}}, \lambda_{\text{feat}}, \lambda_{\text{adv}} \in \mathbb{R}_{++}$  are hyperparameters. The per-pixel loss  $\mathcal{L}_{\text{pix}}(\phi)$  is the  $\ell_1$  distance between prediction  $\mathcal{G}_{\phi}(f)$  and target  $x$ . The perceptual loss  $\mathcal{L}_{\text{feat}}(\phi, \tilde{\theta})$  is the  $\ell_2$  distance between the AR features of prediction and target. The adversarial loss  $\mathcal{L}_{\text{adv}}(\phi, \psi)$  maximizes the discriminator score of predictions *i.e.* it increases the chance the discriminator classifies them as real. So, the generator is trained to create images with a discriminator output close

to 1. Optimal discriminator weights are obtained via the cross-entropy loss  $\min_{\psi} \mathcal{L}_{\text{disc}}(\phi, \psi)$ , where:

$$\mathcal{L}_{\text{disc}}(\phi, \psi) \triangleq \mathbb{E}_{x \sim \tilde{\mathcal{K}}} [-\log D_{\psi}(x) - \log(1 - D_{\psi} \circ \mathcal{G}_{\phi}(f))]. \quad (7)$$

The discriminative loss  $\mathcal{L}_{\text{disc}}(\phi, \psi)$  guides the discriminator to maximize the score of real images and minimize the score of reconstructed (fake) images. Similar to traditional GAN algorithms, we alternate between the generator and discriminator training to reach the equilibrium point.

### 3.3. Applications

Our AR autoencoder can be harnessed to improve the performance of applications such as deep anomaly detection [9], universal style transfer [32], and image denoising [58].

**Anomaly Detection.** Anomaly detection consists in identifying samples that do not fit an expected pattern [9, 20, 49, 59]. Given an unlabeled dataset with normal and anomalous instances, the goal is to distinguish between them. Following GAN-based *one-vs-all* techniques [9], we train an AR autoencoder on normal instances to learn how to accurately reconstruct them (See Sec. A3.2 for details on the training setup). Once trained on the target distribution, we use its reconstruction accuracy to detect outliers.

Given an unlabeled sample  $x$  and its AR features  $f$ , we search for the latent code  $\hat{f}$  that yields the best reconstruction  $\hat{x} = G_{\tilde{\phi}}(\hat{f})$  based on the following criterion (Fig. 2b):

$$\hat{f} = \arg \min_f \alpha_{\text{pix}} \|G_{\tilde{\phi}}(f) - x\|_1 + \alpha_{\text{feat}} \|F_{\tilde{\theta}} \circ G_{\tilde{\phi}}(f) - F_{\tilde{\theta}}(x)\|_2^2, \quad (8)$$

where  $\alpha_{\text{pix}}, \alpha_{\text{feat}} \in \mathbb{R}_{++}$  are hyperparameters. Basically,  $x$  is associated to  $\hat{f}$  that minimizes per-pixel and perceptual losses between estimation and target. Since  $G_{\tilde{\phi}}$  has been trained on the target distribution, latent codes of negative instances should generate abnormal reconstructions.

**Example-based Style Transfer.** Style transfer [19] aligns deep representations to impose perceptual properties of the style image over semantic properties of the content image. We adopt the Universal Style Transfer framework [32] to show the benefits of AR features for stylization.

Taking as example the AlexNet model, we train three AR autoencoders, denoted by  $\{F_{l,\tilde{\theta}}, G_{l,\tilde{\phi}}\}_{l=1}^{L=3}$ , to sequentially align features at different pooling levels (Fig. 2c). The first autoencoder provides access to AR AlexNet conv1 features. Similarly, the second and third autoencoders provide access to conv2 and conv5 features, respectively. See Sec. A3.3 for the training details of each autoencoder.

Given a content image  $x_c$  and a style image  $x_s$ , the stylized image  $x_{cs}^L$  corresponds to the third autoencoder output. We denote the  $l$ -th autoencoder output as  $x_{cs}^l \triangleq G_{l,\tilde{\phi}}(f_t^l)$ ,



where  $f_t^l \triangleq \mathcal{T}(f_s^l, f_{cs}^l)$  are the aligned features obtained by transforming style and stylized features,  $f_s^l \triangleq F_{l,\tilde{\theta}}(x_s)$  and  $f_{cs}^l \triangleq F_{l,\tilde{\theta}}(x_{cs}^{l-1})$  respectively, via the feature transform denoted by  $\mathcal{T}$  [32]. Notice that  $x_{cs}^0 = x_c$ .

**Image Denoising.** Similar to denoising autoencoders (DAE) [58] where meaningful features are extracted from distorted instances, we leverage AR features for image denoising. Motivated by deep denoising models [37], skip connections are included to access features at different encoding levels (Fig. 2d), to better preserve details and complement the encoder bottleneck (See Sec. A3.4 for the training details). Skip connections correspond to Wavelet Pooling [60], replacing pooling and upsampling layers by analysis and synthesis Haar wavelet operators, respectively. Our skip-connected model is denoted by pair  $\{F_{s,\tilde{\theta}}, G_{s,\tilde{\phi}}\}$ .

We consider the image range to be limited, which aligns with real quantization scenarios [14, 39, 62]. Let a noisy image be denoted by  $b \triangleq \rho(x + \eta) \in \mathbb{R}^{W \times H \times C}$ , where  $x$  is the clean image,  $\eta \sim \mathcal{N}(0, \sigma)$  the additive white Gaussian noise term and  $\rho(x) \triangleq \max[0, \min(1, x)]$  a pointwise operator restricting the range between 0 and 1. Then, predictions correspond to  $\hat{x}_s \triangleq G_{s,\tilde{\phi}} \circ F_{s,\tilde{\theta}}(b)$ .

## 4. Experiments on Feature Inversion

### 4.1. Reconstruction Accuracy of AR Autoencoders

We begin by analyzing the reconstruction quality achieved by inverting representations from different encoders and empirically show that learning how to invert AR features via our proposed image generator attains a significant improvement over standard feature inversion.

**Inverting AlexNet features.** Standard and AR AlexNet features are inverted using our proposed model. Similar to alternative methods [11], generators are trained on ImageNet using (i) Per-pixel, (ii) Per-pixel and feature, and (iii) Per-pixel, feature and GAN losses to understand the impact of inverting AR representations. Reconstruction accuracy is evaluated using PSNR, SSIM and LPIPS.

Standard and AR models were trained using cross-entropy loss and  $\ell_2$ -PGD attacks ( $\varepsilon = \frac{3}{255}$ ), respectively. PGD settings were chosen to give the best balance between PSNR, SSIM and LPIPS improvement, as covered in Sec. 4.2 (See Sec. A3.1 for full training details).

Reconstructions from AR features obtain better PSNR and SSIM values than their standard counterparts under all three criteria (Tab. 1). LPIPS scores are also consistently better, except when using pixel, feature and GAN losses. Nevertheless, in this case AR features obtain a significant PSNR and SSIM increase. Overall, decoding AR features better preserves the natural structure for all losses (Fig. 3).

**Inverting VGG features.** We extend our feature inversion analysis to VGG-16 and evaluate the improvement achieved by learning how to invert its AR features. We use

Losses	Model	PSNR (dB)↑	SSIM↑	LPIPS↓
$\mathcal{L}_{\text{pix}}$	Std	17.562 ± 2.564	0.454 ± 0.167	0.624 ± 0.099
	AR	<b>19.904 ± 2.892</b>	<b>0.505 ± 0.169</b>	<b>0.596 ± 0.104</b>
$\mathcal{L}_{\text{pix}}, \mathcal{L}_{\text{feat}}$	Std	14.462 ± 1.884	0.103 ± 0.044	0.713 ± 0.046
	AR	<b>17.182 ± 2.661</b>	<b>0.284 ± 0.111</b>	<b>0.601 ± 0.034</b>
$\mathcal{L}_{\text{pix}}, \mathcal{L}_{\text{feat}}, \mathcal{L}_{\text{adv}}$	Std	15.057 ± 2.392	0.307 ± 0.158	0.547 ± 0.055
	AR	<b>17.227 ± 2.725</b>	<b>0.358 ± 0.163</b>	<b>0.567 ± 0.056</b>

Table 1. AlexNet feature inversion on ImageNet. Under distinct training losses, inverting AR features via our proposed generator is consistently more accurate than inverting standard features.

	Standard Model	AR Model (ours)
Standard Accuracy	65.0	48.7
$\ell_\infty$ PGD Attack	0	23.0
PSNR (dB) ↑	18.35 ± 2.471	<b>21.063 ± 3.132</b>
SSIM ↑	0.466 ± 0.17	<b>0.538 ± 0.165</b>
LPIPS ↑	0.327 ± 0.101	<b>0.225 ± 0.057</b>

Table 2. VGG-16 feature inversion on ImageNet. By training our generator using per-pixel and feature losses, a significant reconstruction improvement is obtained from AR representations.

the pre-trained encoder weights from the recent work by Liu et al. [33], where the AR model is trained using  $\ell_\infty$  PGD attacks ( $\varepsilon = 0.01$ ), and compare its accuracy against the standard version trained via cross-entropy loss. Both models were trained on ImageNet-143.

We consider VGG-16 up to its conv5.1 layer ( $14 \times 14 \times 512$ ) and train generators via per-pixel and feature losses. Reconstruction accuracy and robustness of each model using  $\ell_\infty$  PGD attacks ( $\varepsilon = 0.01$ ) is reported (see Tab. 2).

Results indicate that reconstructing images from AR VGG-16 representations outperforms standard ones by a large margin. Furthermore, it significantly improves the reconstruction accuracy obtained by inverting AR AlexNet representations. These suggest that the benefits of inverting AR features are not constrained to shallow models such as AlexNet, but generalize to more complex ones.

**Inverting ResNet features.** We evaluate the reconstruction obtained by a state-of-the-art AR classifier, as ranked by RobustBench [7]: The WideResNet-28-10 model trained via *geometry-aware instance-reweighted adversarial training* (GAIRAT) [61]. We invert AR features of its 3rd residual block ( $8 \times 8 \times 640$ ) and compare its accuracy to that of its standard version trained via cross-entropy loss.

Standard and AR generators are fully trained via per-pixel and feature losses on CIFAR10. Reconstruction accuracy and robustness via AutoAttack [8] is reported for both models (see Tab. 3). Inverting AR features shows a large improvement over standard ones. This enforces our claim that the benefits of inverting AR features not only extend to different models, but also datasets and training strategies.

### 4.2. Relationship Between Robustness Level and Reconstruction Accuracy

To analyze the effect of adversarial robustness in the inversion accuracy, we invert five different AlexNet classi-



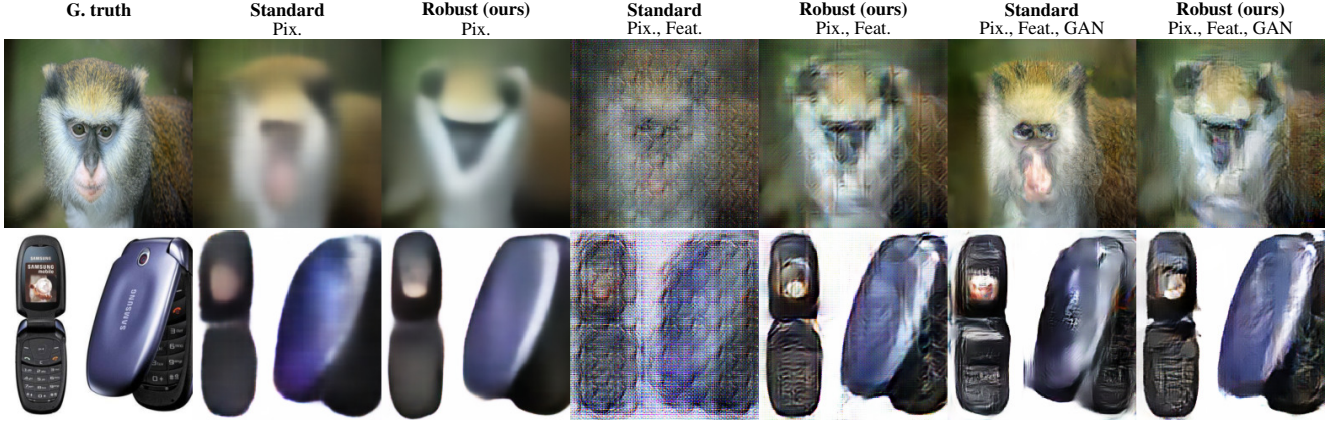


Figure 3. Feature inversion via standard and AR representations. AlexNet conv5 features are inverted using our proposed generator trained on ImageNet. Under three different training criteria, reconstructions from AR features are more faithful to the ground-truth image.

	Standard Model	AR Model (ours)
Standard Accuracy	93.8	89.36
AutoAttack [8]	0	59.64
PSNR (dB) $\uparrow$	$17.38 \pm 2.039$	<b><math>22.14 \pm 1.626</math></b>
SSIM $\uparrow$	$0.59 \pm 0.1$	<b><math>0.81 \pm 0.067</math></b>
LPIPS $\downarrow$	$0.2547 \pm 0.055$	<b><math>0.2318 \pm 0.0833</math></b>

Table 3. WideResNet-28-10 [61] inversion on CIFAR-10. inverting AR features using our generator trained on per-pixel and feature losses shows a significant reconstruction improvement.

	$\ell_2$ PGD Attack ( $\epsilon$ )				
	0	0.5	2	3	4
Standard Accuracy	53.69	49.9	43.8	39.83	36.31
AutoAttack [8]	8.19	48.0	28.0	22.27	14.9
	( $\epsilon = 0.5$ )	( $\epsilon = 0.5$ )	( $\epsilon = 2$ )	( $\epsilon = 3$ )	( $\epsilon = 4$ )
PSNR (dB) $\uparrow$	13.12	14.41	15.5	15.53	<b>15.61</b>
SSIM $\uparrow$	0.20	0.26	<b>0.3</b>	0.26	0.25
LPIPS $\downarrow$	0.657	0.625	<b>0.614</b>	0.629	0.644

Table 4. Reconstruction vs. Robustness. Experiments on ImageNet show that learning to invert AlexNet features with different AR levels significantly affects the reconstruction accuracy.

fiers, one standard and four AR models, trained on ImageNet using  $\ell_2$  PGD attacks ( $\epsilon \in \{0.5, 2, 3, 4\}/255$ ). Generators are trained via per-pixel, feature and GAN losses and evaluated in terms of PSNR, SSIM and LPIPS values. Parameter-free attacks via AutoAttack are also generated with the same attack radius used during training (see Tab. 4) to reliably measure the robustness of each model.

Results show LPIPS and SSIM improve almost monotonically until a maximum value is reached, while PSNR keeps increasing. These suggest that the inversion accuracy is not proportional to the robustness level. Instead, it is maximized at a particular level. See Sec. A1.3 for additional ResNet-18 experiments pointing to the same conclusion.

### 4.3. Reconstructing Images at Unseen Scales

Unlike extracting shift-invariant representations, image scaling is difficult to handle for standard CNN-based mod-

$L$	Standard AlexNet			AR AlexNet (ours)		
	PSNR (dB) $\uparrow$	SSIM $\uparrow$	LPIPS $\downarrow$	PSNR (dB) $\uparrow$	SSIM $\uparrow$	LPIPS $\downarrow$
1	15.057	0.307	0.547	17.227	0.358	0.567
4	15.426	0.466	0.414	22.575	0.589	0.401
7	13.892	0.485	0.459	23.578	0.659	0.39
10	13.101	0.497	0.486	23.957	0.724	0.389

Table 5. Reconstructing upscaled images from their features. Contrary to the standard case, inverting AR AlexNet features of upscaled ImageNet samples monotonically increase with scale, leading to a substantial improvement.

els [18, 56]. Since AR features are more generic and transferable [5, 51], we test whether our proposed AR autoencoder generalizes better to scale changes. In contrast to standard inversion, our model trained on low-res samples attains exceptionally good reconstructions of images at unseen scales without any fine-tuning. We explore this property on our proposed AR AlexNet model.

**Scenario 1: Reconstructing Upscaled Images.** Upscaled ImageNet samples are reconstructed from their AR AlexNet conv5 representations. For a fair comparison across scales, each image is normalized to  $224 \times 224$  px. and then enlarged by an integer factor  $L > 1$ . Substantially higher accuracy is obtained using AR features in terms of PSNR, SSIM and LPIPS (Tab. 5). All metrics improve almost monotonically with  $L$ . In contrast, accuracy using standard features degrades with  $L$  (see Sec. A1.2 for full experimental results). Inversion from AR features show almost perfect reconstruction for large scales, while those of standard features show severe distortions (Fig. 4).

**Scenario 2: Reconstructing High-Resolution Images.** Standard and AR feature inversion is performed on the DIVerse 2K resolution dataset (DIV2K) [1], containing images of objects at multiple scales. AR feature reconstructions show a significant PSNR, SSIM and LPIPS improvement over standard ones (Fig. 5), despite not being explicitly trained to handle such large-scale objects (Tab. 6). This

	Standard AlexNet	AR AlexNet (ours)
PSNR (dB) $\uparrow$	14.266 $\pm$ 1.9015	<b>18.3606<math>\pm</math> 2.6012</b>
SSIM $\uparrow$	0.3874 $\pm$ 0.151	<b>0.4388<math>\pm</math> 0.1508</b>
LPIPS $\downarrow$	0.5729 $\pm$ 0.0465	<b>0.5673<math>\pm</math> 0.0337</b>

Table 6. Reconstructing high-resolution images from their features. Despite trained on a low-resolution regime, inverting AR AlexNet features of DIV2K samples attains a significant reconstruction improvement without any fine-tuning.

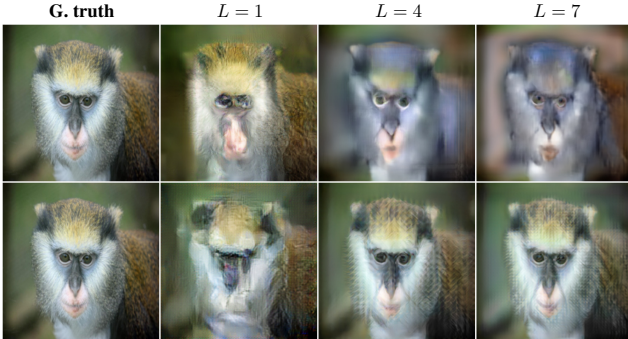


Figure 4. Upscaled ImageNet samples are inverted from their standard and AR features. While standard reconstructions (top row) are severely degraded, AR reconstructions (bottom row) show an outstanding accuracy that improves with the scaling factor.

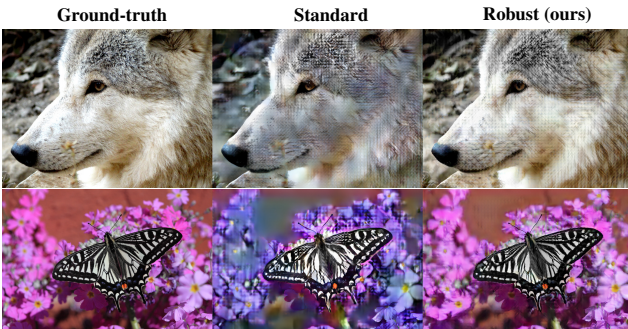


Figure 5. At a resolution of  $2040 \times 1536$ , 10 times higher than in training, standard reconstructions show color and structure degradation. In contrast, reconstructions from our AR autoencoder do not suffer from distortions and are closer to target DIV2K images.

indicates that, for unseen scales and without finetuning, AR features better preserve structure without penalizing the perceptual similarity (additional results are in Sec. A1.2).

#### 4.4. Comparison against State-of-the-Art Feature Inversion Techniques

The inversion accuracy of our proposed AR autoencoder is compared against two alternative techniques: Optimization-based robust representation inversion (RI) [16] and DeePSiM [11]. We focus on reconstructing images from their AR AlexNet features. While RI searches over the pixel domain relying exclusively on deep feature matching, we use a CNN-based generator trained on a combination of natural-image priors (Sec. 3.2). On the other hand, while DeePSiM is also a model-based technique trained under

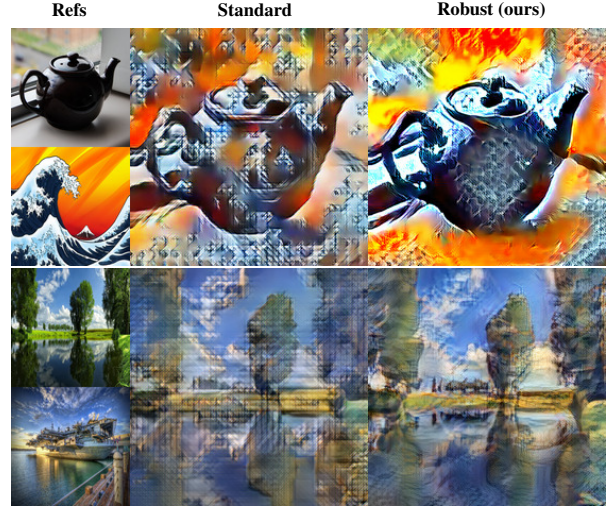


Figure 6. Universal Style Transfer: By inverting AR features, our autoencoder significantly improves both content and style preservation, obtaining a better image stylization.

multiple priors, its generator has approximately 63% more trainable parameters than ours (Tab. 7). We compare against their results inverting CaffeNet [26].

**Experimental Setup.** All inversion methods are evaluated on ImageNet. DeePSiM settings are those of its official Caffe implementation. Standard and AR models are trained using per-pixel, feature and GAN losses. Input samples are rescaled to  $224 \times 224$  px. ( $227 \times 227$  px. for DeePSiM). On the other hand, RI is evaluated using its official Pytorch implementation, modified to invert conv5 robust features.

**Results.** Our AR AlexNet autoencoder obtains the best accuracy in terms of PSNR and the second best in terms of SSIM (Tab. 7). While it outperforms its standard version in PSNR and SSIM, it gets a marginally worse LPIPS. Moreover, our AR model outperforms RI in all three metrics. Also, despite DeePSiM pre-trained model having more layers and using larger images, our model achieves a significant PSNR improvement over it. See Sec. A1.4 for additional training details and reconstruction results.

## 5. Downstream Tasks

### 5.1. Anomaly Detection using AR Representations

We hypothesize that our AR generator widens the reconstruction gap between in and out-of-distribution samples, improving its anomaly detection performance. Following this, we evaluate our AR model on *one-vs-all* classification.

**Experimental Setup.** Given a multiclass labeled dataset, our generator is trained to invert AR features from samples of a single class (*positives*). Performance is measured by how accurately samples from other classes (*negatives*) are distinguished from positives on an unlabeled dataset via AUROC. Experiments are performed on CIFAR10 [30] and Cats vs. Dogs [45] datasets. Detection



Algorithm	Method	Encoder	Pars.	PSNR (dB) $\uparrow$	SSIM $\uparrow$	LPIPS $\downarrow$
RI [16]	Optim.	AR AlexNet	—	$16.724 \pm 2.434$	$0.181 \pm 0.071$	$0.63 \pm 0.04$
Standard Autoencoder	CNN	Std AlexNet	4.7M	$15.057 \pm 2.392$	$0.307 \pm 0.158$	<b><math>0.547 \pm 0.055</math></b>
Ours	CNN	AR AlexNet	4.7M	<b><math>17.227 \pm 2.725</math></b>	<b><math>0.358 \pm 0.163</math></b>	$0.567 \pm 0.056$
DeepSiM [12]	CNN	Std CaffeNet	12.7M	$15.321 \pm 2.011$	$0.417 \pm 0.158$	$0.531 \pm 0.059$

Table 7. Comparison against state-of-the-art inversion techniques. By learning how to invert AR features, our autoencoder outperforms the optimization-based RI approach by a large margin. Despite having 63% less parameters, ours obtains favorable results against the pre-trained DeepSiM, showing a significant PSNR improvement.

is performed on their full test sets. The latent code is initialized as random Gaussian noise and optimized for 100 iterations using per-pixel and feature losses.

**Results.** We compare our technique, using both standard and AR features, against the Anomaly Detection with GANs (ADGAN) method [9, 20]. On average, our AR model obtains larger AUROC in both datasets (Tab. 8). For CIFAR10, it obtains 1.61% and 6.51% relative increases over its standard version and ADGAN, respectively. For Cats vs. Dogs, it obtains 1.99% and 8.84% relative increases over its standard version and ADGAN, respectively. See Sec. A2.1 for full anomaly detection results.

## 5.2. Style Transfer via Robust Feature Alignment

Motivated by the perceptual properties of AR features [16], we analyze their impact on style transfer using our AR AlexNet autoencoder as backbone and measure their improvement in both structure and texture preservation.

**Experimental Setup.** Multi-level stylization is evaluated using 75 random content images from the MS COCO dataset and 100 random style images from the Wikiart dataset. Performance is evaluated via the SSIM between content and stylized images and the VGG-19 Gram loss between style and stylized images, respectively. To reduce artifacts, conv1 and conv2 models use nearest neighbor interpolation, while conv5 model remains unaltered. We use the official Universal Style Transfer (UST) implementation (VGG-19 backbone) as reference.

**Results.** The AR model drastically improves both texture and structure preservation over standard features (Tab. 9). Stylization via AR features removes artifacts in flat areas, reducing blurry outputs and degraded structure (Fig. 6). Besides, our AR model gets a lower Gram loss than UST. This implies that, despite matching less maps than the VGG-19 model, three instead of five, stylizing via our AR autoencoder is more faithful to the target style.

As expected, UST obtains a better SSIM because VGG-19 has more parameters and uses less contracted feature maps than our model (e.g.  $14 \times 14 \times 512$  vs.  $6 \times 6 \times 256$ ). Also, UST *blends* stylized and content images to better preserve shapes. Overall, a comparison between our AR model

Dataset	ADGAN [9]	Std	Ours
CIFAR10	0.553	0.58	<b>0.589</b>
Cats vs. Dogs	0.494	0.527	<b>0.538</b>

Table 8. One-versus-all anomaly detection using AR representations. Our proposed GAN-based method based on AR features outperforms both its standard counterpart and the state-of-the-art ADGAN method on multiple datasets, attaining superior AUROC  $\uparrow$ .

Encoder	Stages	Smallest Feature Map	Blend	Gram Loss $\downarrow$ ( $x_{cs}, x_s$ )	SSIM $\uparrow$ ( $x_{cs}, x_c$ )
Standard AlexNet	3	$6 \times 6 \times 2^8$	$\times$	1.694	0.226
AR (ours)	3	$6 \times 6 \times 2^8$	$\times$	<b>1.186</b>	<b>0.259</b>
VGG-19 [55]	5	$14 \times 14 \times 2^9$	$\checkmark$	1.223	0.459

Table 9. Universal Style Transfer using AR representations. Our robust AlexNet autoencoder outperforms both its standard counterpart and the original VGG-19 model in terms of Gram loss; the latter using more layers, larger feature maps and feature blending.

		TNRD [6]	MLP [4]	Standard	Ours
CBSD68	PSNR (dB) $\uparrow$	24.75	25.184	22.63	<b>25.258</b>
	SSIM $\uparrow$	0.662	0.663	0.618	<b>0.71</b>
	LPIPS $\downarrow$	0.445	0.46	0.567	<b>0.404</b>
Kodak24	PSNR (dB) $\uparrow$	25.994	<b>26.31</b>	23.187	25.495
	SSIM $\uparrow$	0.695	0.691	0.6	<b>0.701</b>
	LPIPS $\downarrow$	0.461	0.478	0.497	<b>0.447</b>
McMaster	PSNR (dB) $\uparrow$	25.01	<b>26.039</b>	23.149	25.353
	SSIM $\uparrow$	0.66	0.693	0.607	<b>0.691</b>
	LPIPS $\downarrow$	<b>0.387</b>	0.402	0.446	0.397

Table 10. Image denoising ( $\sigma = \frac{50}{255}$ ): Our AR denoiser outperforms its standard version on multiple datasets. On the largest one (CBSD68), it also outperforms alternative learn-based techniques. On smaller sets (Kodak24, McMaster), it significantly improves in SSIM and gets comparable PSNR and LPIPS performance.

and UST shows a tradeoff between content and style preservation. See Sec. A2.2 for additional stylization results.

## 5.3. Image Denoising

Similar to the robustness imposed by regularized autoencoders [29, 48, 58], we harness the manifold learned by AR models to obtain noise-free reconstructions. We evaluate our AR Alexnet denoising model and compare its restoration properties with alternative learn-based methods.

**Experimental Setup.** Skip connections are included in conv1, conv2 and conv5 layers. Generators are trained on ImageNet using pixel and feature losses. Accuracy is evaluated on the Kodak24, McMaster and Color Berkeley Segmentation Dataset 68 (CBSD68) for additive Gaussian



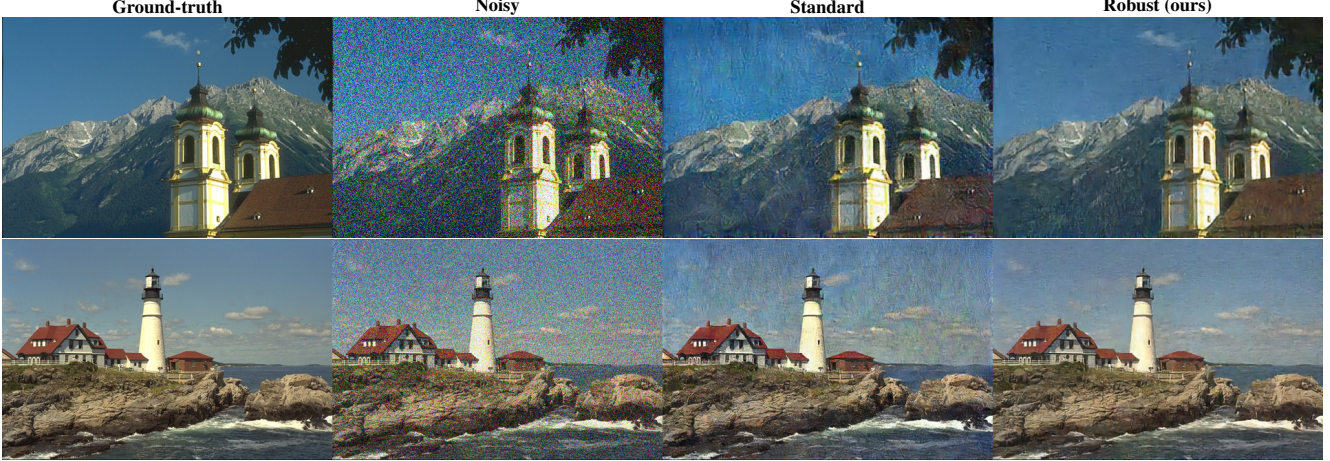


Figure 7. Image denoising ( $\sigma = \frac{50}{255}$ ): While inverting standard features introduces artifacts and degrades the output color, disallowing their use for restoration purposes, our AR denoiser substantially reduces the artifacts and better preserves the original texture.

noise ( $\sigma = 50/255$ ). We compare our denoising technique against two alternative model-based approaches, Trainable Nonlinear Reaction Diffusion (TNRD) [6] and Multi Layer Perceptron-based approach (MLP) [4], both often included in real-noise denoising benchmarks [2, 23].

**Results.** For all datasets, our robust model shows a substantial reconstruction improvement in all metrics across all datasets (Tab. 10). While standard predictions include color distortions and notorious artifacts, robust predictions show a better texture preservation and significantly reduce the distortions introduced by the denoising process (Fig. 7).

Our AR model obtains the best PSNR, SSIM and LPIPS scores on CBSD68, the most diverse of all evaluated sets. While it is outperformed in PSNR by MLP in the two remaining datasets, it consistently improves in SSIM and LPIPS. For the McMaster dataset, TNRD and our AR model achieve comparable LPIPS. Overall, our model consistently preserves the perceptual and structural similarity across sets, outperforming the alternative data-driven approaches.

## 6. Related Work

**Inverting Neural Networks.** Prior work exploring deep feature inversion using optimization approaches are either limited to per-pixel priors or require multiple steps to converge and are sensitive to initialization [16, 35, 36, 52]. Instead, we propose to map contracted features to images via a generator, following the work by Dosovitskiy et al. [12] and similar synthesis techniques [41, 42, 53]. By combining natural priors and AR features, we get a significant reconstruction improvement with much less trainable parameters.

Our results are consistent to prior findings on AR features being more invertible via optimization [16] and more useful for transfer learning [51]. We complement these by showing that (i) learning a map from the AR feature space to the image domain largely outperforms the original optimization approach, (ii) such an improvement generalizes to

models of different complexity, and (iii) inverting AR features shows remarkable robustness to scale changes. We also show AR encoders with higher robustness can be more easily decoded, revealing potential security issues [64].

**Regularized Autoencoders.** Prior work requiring data augmentation to train generative and autoencoding models often requires learning an invertible transformation that maps augmented samples back to real data [28]. Instead, our approach can be seen as a novel way to regularize bottleneck features, providing an alternative to contractive, variational and sparse autoencoders [21, 29, 40].

## 7. Discussions and Conclusions

A novel encoding-decoding model for synthesis tasks is proposed by exploiting the perceptual properties of AR features. We show the remarkable reconstruction obtained by generators trained on AR features and how it generalizes to models of different complexity. We use our model on three applications: anomaly detection, style transfer and image denoising, outperforming standard approaches and attaining competitive performance with alternative methods. A potential limitation of our model is the spatial information loss due to its contracted features. Yet, denoising experiments show that shortcut connections can be used to preserve details, enabling enhancement and restoration tasks.

Based on their performance, AR features can be extended to conditional GANs for image-to-image translation tasks [25]. They can also be used in the VAE framework as a latent variable regularizer [12]. Similarly, our AR autoencoder can be seen as an energy-based model, *e.g.* a Plug and Play Generative Net [41], enabling tasks such as visualizing artificial and biological neural networks [42, 43, 46].

## Acknowledgement

AN was supported by the NSF Grant No. 1850117 and a donation from NaphCare Foundation. We are grateful for Kelly Price’s tireless assistance with our GPU servers at Auburn University.

## References

- [1] Eirikur Agustsson and Radu Timofte. Ntire 2017 challenge on single image super-resolution: Dataset and study. In *Proceedings of the IEEE Conference on Computer Vision and Pattern Recognition Workshops*, pages 126–135, 2017.
- [2] Saeed Anwar and Nick Barnes. Real image denoising with feature attention. In *Proceedings of the IEEE/CVF International Conference on Computer Vision*, pages 3155–3164, 2019.
- [3] Anish Athalye, Nicholas Carlini, and David Wagner. Obfuscated gradients give a false sense of security: Circumventing defenses to adversarial examples. *arXiv preprint arXiv:1802.00420*, 2018.
- [4] Harold C Burger, Christian J Schuler, and Stefan Harmeling. Image denoising: Can plain neural networks compete with bm3d? In *2012 IEEE conference on computer vision and pattern recognition*, pages 2392–2399. IEEE, 2012.
- [5] Peijie Chen, Chirag Agarwal, and Anh Nguyen. The shape and simplicity biases of adversarially robust imagenet-trained cnns. *arXiv preprint arXiv:2006.09373*, 2020.
- [6] Yunjin Chen and Thomas Pock. Trainable nonlinear reaction diffusion: A flexible framework for fast and effective image restoration. *IEEE transactions on pattern analysis and machine intelligence*, 39(6):1256–1272, 2016.
- [7] Francesco Croce, Maksym Andriushchenko, Vikash Sehwag, Nicolas Flammarion, Mung Chiang, Prateek Mittal, and Matthias Hein. Robustbench: a standardized adversarial robustness benchmark. *arXiv preprint arXiv:2010.09670*, 2020.
- [8] Francesco Croce and Matthias Hein. Reliable evaluation of adversarial robustness with an ensemble of diverse parameter-free attacks. In *International conference on machine learning*, pages 2206–2216. PMLR, 2020.
- [9] Lucas Deecke, Robert Vandermeulen, Lukas Ruff, Stephan Mandt, and Marius Kloft. Image anomaly detection with generative adversarial networks. In *Joint european conference on machine learning and knowledge discovery in databases*, pages 3–17. Springer, 2018.
- [10] Jeff Donahue and Karen Simonyan. Large scale adversarial representation learning. 2019.
- [11] Alexey Dosovitskiy and Thomas Brox. Inverting convolutional networks with convolutional networks. *arXiv preprint arXiv:1506.02753*, 4, 2015.
- [12] Alexey Dosovitskiy and Thomas Brox. Generating images with perceptual similarity metrics based on deep networks. In *Advances in neural information processing systems*, pages 658–666, 2016.
- [13] A. Dosovitskiy and T. Brox. Inverting visual representations with convolutional networks. In *CVPR*, 2016.
- [14] Majed El Helou and Sabine Süsstrunk. Blind universal bayesian image denoising with gaussian noise level learning. *IEEE Transactions on Image Processing*, 29:4885–4897, 2020.
- [15] Logan Engstrom, Andrew Ilyas, Hadi Salman, Shibani Santurkar, and Dimitris Tsipras. Robustness (python library), 2019.
- [16] Logan Engstrom, Andrew Ilyas, Shibani Santurkar, Dimitris Tsipras, Brandon Tran, and Aleksander Madry. Adversarial robustness as a prior for learned representations. *arXiv preprint arXiv:1906.00945*, 2019.
- [17] Patrick Esser, Robin Rombach, and Bjorn Ommer. Taming transformers for high-resolution image synthesis. In *Proceedings of the IEEE/CVF Conference on Computer Vision and Pattern Recognition*, pages 12873–12883, 2021.
- [18] Yuchen Fan, Jiahui Yu, Ding Liu, and Thomas S Huang. Scale-wise convolution for image restoration. In *Proceedings of the AAAI Conference on Artificial Intelligence*, volume 34, pages 10770–10777, 2020.
- [19] Leon A Gatys, Alexander S Ecker, and Matthias Bethge. Image style transfer using convolutional neural networks. In *Proceedings of the IEEE conference on computer vision and pattern recognition*, pages 2414–2423, 2016.
- [20] Izhak Golan and Ran El-Yaniv. Deep anomaly detection using geometric transformations. *arXiv preprint arXiv:1805.10917*, 2018.
- [21] Ian Goodfellow, Yoshua Bengio, and Aaron Courville. Deep learning book. *MIT Press*, 521(7553):800, 2016.
- [22] Ian J Goodfellow, Jonathon Shlens, and Christian Szegedy. Explaining and harnessing adversarial examples. *arXiv preprint arXiv:1412.6572*, 2014.
- [23] Shi Guo, Zifei Yan, Kai Zhang, Wangmeng Zuo, and Lei Zhang. Toward convolutional blind denoising of real photographs. In *Proceedings of the IEEE/CVF Conference on Computer Vision and Pattern Recognition*, pages 1712–1722, 2019.
- [24] Kaiming He, Xiangyu Zhang, Shaoqing Ren, and Jian Sun. Deep residual learning for image recognition. In *Proceedings of the IEEE conference on computer vision and pattern recognition*, pages 770–778, 2016.
- [25] Phillip Isola, Jun-Yan Zhu, Tinghui Zhou, and Alexei A Efros. Image-to-image translation with conditional adversarial networks. In *Proceedings of the IEEE conference on computer vision and pattern recognition*, pages 1125–1134, 2017.
- [26] Yangqing Jia, Evan Shelhamer, Jeff Donahue, Sergey Karayev, Jonathan Long, Ross Girshick, Sergio Guadarrama, and Trevor Darrell. Caffe: Convolutional architecture for fast feature embedding. In *Proceedings of the 22nd ACM international conference on Multimedia*, pages 675–678, 2014.
- [27] Justin Johnson, Alexandre Alahi, and Li Fei-Fei. Perceptual losses for real-time style transfer and super-resolution. In *European conference on computer vision*, pages 694–711. Springer, 2016.
- [28] Heewoo Jun, Rewon Child, Mark Chen, John Schulman, Aditya Ramesh, Alec Radford, and Ilya Sutskever. Distribution augmentation for generative modeling. In *International Conference on Machine Learning*, pages 5006–5019. PMLR, 2020.
- [29] Diederik P Kingma and Max Welling. Auto-encoding variational bayes. *arXiv preprint arXiv:1312.6114*, 2013.

- [30] Alex Krizhevsky, Geoffrey Hinton, et al. Learning multiple layers of features from tiny images. 2009.
- [31] Alex Krizhevsky, Ilya Sutskever, and Geoffrey E Hinton. Imagenet classification with deep convolutional neural networks. In *Advances in neural information processing systems*, pages 1097–1105, 2012.
- [32] Yijun Li, Chen Fang, Jimei Yang, Zhaowen Wang, Xin Lu, and Ming-Hsuan Yang. Universal style transfer via feature transforms. In *Proceedings of the 31st International Conference on Neural Information Processing Systems, NIPS’17*, page 385–395, Red Hook, NY, USA, 2017. Curran Associates Inc.
- [33] Xuanqing Liu, Yao Li, Chongruo Wu, and Cho-Jui Hsieh. Adv-bnn: Improved adversarial defense through robust bayesian neural network. *arXiv preprint arXiv:1810.01279*, 2018.
- [34] Aleksander Madry, Aleksandar Makelov, Ludwig Schmidt, Dimitris Tsipras, and Adrian Vladu. Towards deep learning models resistant to adversarial attacks. iclr. *arXiv preprint arXiv:1706.06083*, 2018.
- [35] Aravindh Mahendran and Andrea Vedaldi. Understanding deep image representations by inverting them. In *Proceedings of the IEEE conference on computer vision and pattern recognition*, pages 5188–5196, 2015.
- [36] Aravindh Mahendran and Andrea Vedaldi. Visualizing deep convolutional neural networks using natural pre-images. *International Journal of Computer Vision*, 120(3):233–255, 2016.
- [37] Xiao-Jiao Mao, Chunhua Shen, and Yu-Bin Yang. Image restoration using very deep convolutional encoder-decoder networks with symmetric skip connections. *arXiv preprint arXiv:1603.09056*, 2016.
- [38] Takeru Miyato, Toshiaki Kataoka, Masanori Koyama, and Yuichi Yoshida. Spectral normalization for generative adversarial networks. *arXiv preprint arXiv:1802.05957*, 2018.
- [39] Michael Moeller, Julia Diebold, Guy Gilboa, and Daniel Cremers. Learning nonlinear spectral filters for color image reconstruction. In *Proceedings of the IEEE International Conference on Computer Vision*, pages 289–297, 2015.
- [40] Andrew Ng et al. Sparse autoencoder. *CS294A Lecture notes*, 72(2011):1–19, 2011.
- [41] Anh Nguyen, Jeff Clune, Yoshua Bengio, Alexey Dosovitskiy, and Jason Yosinski. Plug & play generative networks: Conditional iterative generation of images in latent space. In *Proceedings of the IEEE Conference on Computer Vision and Pattern Recognition*, pages 4467–4477, 2017.
- [42] Anh Nguyen, Alexey Dosovitskiy, Jason Yosinski, Thomas Brox, and Jeff Clune. Synthesizing the preferred inputs for neurons in neural networks via deep generator networks. In *Advances in neural information processing systems*, pages 3387–3395, 2016.
- [43] Anh Nguyen, Jason Yosinski, and Jeff Clune. Understanding neural networks via feature visualization: A survey. In *Explainable AI: interpreting, explaining and visualizing deep learning*, pages 55–76. Springer, 2019.
- [44] Sinno Jialin Pan and Qiang Yang. A survey on transfer learning. *IEEE Transactions on knowledge and data engineering*, 22(10):1345–1359, 2009.
- [45] Omkar M Parkhi, Andrea Vedaldi, Andrew Zisserman, and CV Jawahar. Cats and dogs. In *2012 IEEE conference on computer vision and pattern recognition*, pages 3498–3505. IEEE, 2012.
- [46] Carlos R Ponce, Will Xiao, Peter F Schade, Till S Hartmann, Gabriel Kreiman, and Margaret S Livingstone. Evolving images for visual neurons using a deep generative network reveals coding principles and neuronal preferences. *Cell*, 177(4):999–1009, 2019.
- [47] Ali Razavi, Aaron van den Oord, and Oriol Vinyals. Generating diverse high-fidelity images with vq-vae-2. In *Advances in neural information processing systems*, pages 14866–14876, 2019.
- [48] Salah Rifai, Pascal Vincent, Xavier Muller, Xavier Glorot, and Yoshua Bengio. Contractive auto-encoders: Explicit invariance during feature extraction. In *Icml*, 2011.
- [49] Lukas Ruff, Robert A Vandermeulen, Nico Görmitz, Alexander Binder, Emmanuel Müller, Klaus-Robert Müller, and Marius Kloft. Deep semi-supervised anomaly detection. *arXiv preprint arXiv:1906.02694*, 2019.
- [50] Olga Russakovsky, Jia Deng, Hao Su, Jonathan Krause, Sanjeev Satheesh, Sean Ma, Zhiheng Huang, Andrej Karpathy, Aditya Khosla, Michael Bernstein, et al. Imagenet large scale visual recognition challenge. *International journal of computer vision*, 115(3):211–252, 2015.
- [51] Hadi Salman, Andrew Ilyas, Logan Engstrom, Ashish Kapoor, and Aleksander Madry. Do adversarially robust imagenet models transfer better? *arXiv preprint arXiv:2007.08489*, 2020.
- [52] Shibani Santurkar, Andrew Ilyas, Dimitris Tsipras, Logan Engstrom, Brandon Tran, and Aleksander Madry. Image synthesis with a single (robust) classifier. In *Advances in Neural Information Processing Systems*, pages 1262–1273, 2019.
- [53] Assaf Shocher, Yossi Gandelsman, Inbar Mosseri, Michal Yarom, Michal Irani, William T Freeman, and Tali Dekel. Semantic pyramid for image generation. In *Proceedings of the IEEE/CVF Conference on Computer Vision and Pattern Recognition*, pages 7457–7466, 2020.
- [54] Karen Simonyan, Andrea Vedaldi, and Andrew Zisserman. Deep inside convolutional networks: Visualising image classification models and saliency maps. *arXiv preprint arXiv:1312.6034*, 2013.
- [55] Karen Simonyan and Andrew Zisserman. Very deep convolutional networks for large-scale image recognition. *arXiv preprint arXiv:1409.1556*, 2014.
- [56] Ivan Sosnovik, Michał Szmaja, and Arnold Smeulders. Scale-equivariant steerable networks. *arXiv preprint arXiv:1910.11093*, 2019.
- [57] Dmitry Ulyanov, Andrea Vedaldi, and Victor Lempitsky. Deep image prior. In *Proceedings of the IEEE conference on computer vision and pattern recognition*, pages 9446–9454, 2018.
- [58] Pascal Vincent, Hugo Larochelle, Isabelle Lajoie, Yoshua Bengio, Pierre-Antoine Manzagol, and Léon Bottou. Stacked denoising autoencoders: Learning useful representations in a deep network with a local denoising criterion. *Journal of machine learning research*, 11(12), 2010.
- [59] Siqi Wang, Yijie Zeng, Xinwang Liu, En Zhu, Jianping Yin, Chuanfu Xu, and Marius Kloft. Effective end-to-end unsu-



- pervised outlier detection via inlier priority of discriminative network. In *NeurIPS*, pages 5960–5973, 2019.
- [60] Jaejun Yoo, Youngjung Uh, Sanghyuk Chun, Byeongkyu Kang, and Jung-Woo Ha. Photorealistic style transfer via wavelet transforms. In *Proceedings of the IEEE International Conference on Computer Vision*, pages 9036–9045, 2019.
  - [61] Jingfeng Zhang, Jianing Zhu, Gang Niu, Bo Han, Masashi Sugiyama, and Mohan Kankanhalli. Geometry-aware instance-reweighted adversarial training. *arXiv preprint arXiv:2010.01736*, 2020.
  - [62] Kai Zhang, Wangmeng Zuo, and Lei Zhang. Ffdnet: Toward a fast and flexible solution for cnn-based image denoising. *IEEE Transactions on Image Processing*, 27(9):4608–4622, 2018.
  - [63] Richard Zhang, Phillip Isola, Alexei A Efros, Eli Shechtman, and Oliver Wang. The unreasonable effectiveness of deep features as a perceptual metric. In *Proceedings of the IEEE conference on computer vision and pattern recognition*, pages 586–595, 2018.
  - [64] Yuheng Zhang, Ruoxi Jia, Hengzhi Pei, Wenxiao Wang, Bo Li, and Dawn Song. The secret revealer: Generative model-inversion attacks against deep neural networks. In *Proceedings of the IEEE/CVF Conference on Computer Vision and Pattern Recognition*, pages 253–261, 2020.

# Appendix for: Inverting Adversarially Robust Networks for Image Synthesis

The appendix is organized as follows:

- In Sec. A1, we provide additional results on feature inversion.
- In Sec. A2, we provide more experimental results for the additional applications.
- In Sec. A3, we provide the implementation details and experimental setup.

## A1. Additional Experiments on Feature Inversion

### A1.1. Ablation Study

Feature inversion results obtained by using different optimization criteria are illustrated in Fig. A1. Results clearly show the effect of each term,  $\ell_1$  per-pixel, perceptual and GAN components, in the final reconstruction. Samples correspond to the ImageNet validation set. Particularly, when inverting features using per-pixel and perceptual losses, adversarially robust features show a significant improvement with respect to their standard counterparts. This agrees with the idea of adversarially robust features being perceptually aligned.

### A1.2. Robustness to Scale Changes

Inversion accuracy on upscaled low-resolution images is illustrated in Fig. A2 for scale factors  $L \in \{1, \dots, 10\}$ . While standard inversions show significant distortions for large upscaling factors  $L$ , reconstructions from adversarially robust representations show almost perfect reconstruction for high upscaling factors. Quantitative results for all upscaling factors are included in Tab. A1. Results improve almost monotonically when inverting AR representations, even without exposing the Autoencoder to high-resolution images during training and without any fine-tuning.

On the other hand, extended results on feature inversion from high-resolution images are illustrated in Fig. A3. Notice that, in contrast to the previous case, input samples correspond to originally high-resolution images and are encoded without any spatial pre-processing. Results show a good color and edge preservation from our AR autoencoder, while the inverting standard features show bogus components and noticeable color distortions.

### A1.3. ResNet-18: Robustness Level vs. Reconstruction Accuracy

We take the ResNet-18 model trained on CIFAR-10 from the *Robustness* library [15], invert its third residual block ( $4 \times 4 \times 512$ ) based on our approach using per-pixel and perceptual losses, and evaluate its reconstruction accuracy for standard and AR cases.

We measure the reconstruction accuracy for different robustness levels by training six AR classifiers via  $\ell_2$  PGD attacks (Madry et al.) with attack radii  $\varepsilon$  covering from 0 to 3.5 (see Tab. A2). Accuracy for each model is measured in terms of PSNR, SSIM and LPIPS. We also report the robustness obtained by each model against  $\ell_2$  PGD attacks.

Results show the best accuracy is reached for  $\varepsilon = 2.0$  in terms of PSNR and for  $\varepsilon = 1.5$  in terms of SSIM and LPIPS. Quality increases almost monotonically for models with low robustness and reaches a peak of approximately 19.62 dB PSNR. Models with higher robustness slowly decrease in accuracy, yet obtaining a significant boost w.r.t. the standard model ( $\varepsilon = 0$ ).

### A1.4. Comparison Against Alternative Methods

Feature inversion accuracy obtained by our proposed model is compared against DeePSiM [12] and RI [16] methods. Fig. A4 illustrates the reconstruction accuracy obtained by each method. As previously explained, our generator yields photorealistic results with 37% the trainable parameters required by the DeePSiM generator. Qualitatively, the color distribution obtained by our AR autoencoder is closer to that obtained by DeepSiM. Specifically, without any postprocessing, DeePSiM's results show severe edge distortions, while our method shows minor edge distortions. On the other hand, the optimization based approach from RI introduces several artifacts, despite its use of robust representations. In contrast, our method takes advantage of AR features and minimizes the distortions in a much more efficient manner by replacing the iterative process by a feature inverter (image generator).

Architecture details and training parameters used to train out proposed model are included in Sec. A3.1. DeePSiM results were obtained using its official Caffe implementation. RI results were obtained using its official PyTorch implementation, modified to invert AlexNet conv5 layer.

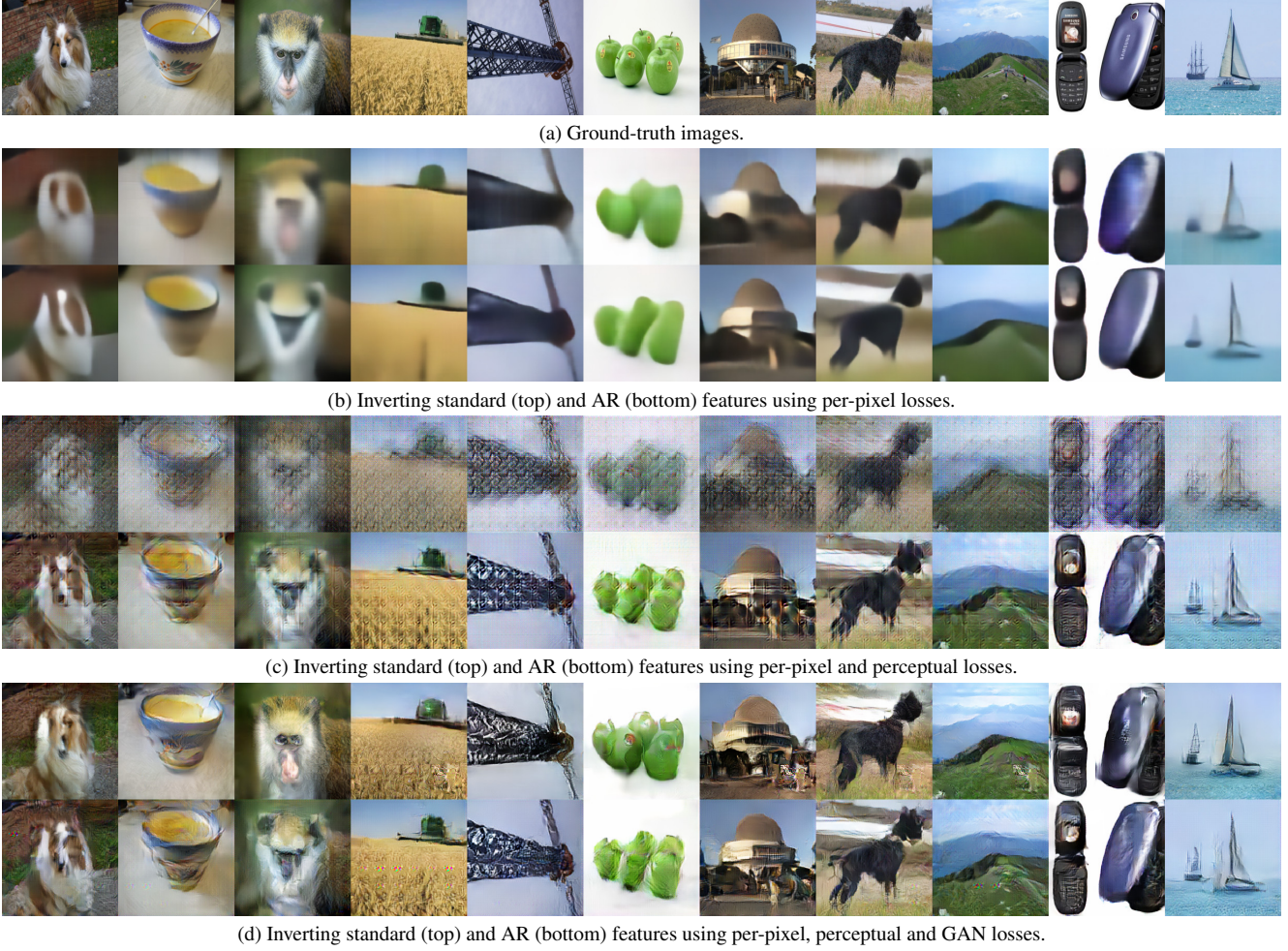


Figure A1. CNN-based feature inversion of standard and AR representations. AlexNet Conv5 **standard** (top) and **AR** (bottom) features are inverted using an image generator trained on (a)  $\ell_1$  Per-pixel loss, (b) Per-pixel and perceptual losses, and (c) Per-pixel, perceptual and GAN losses.

$L$	Standard AlexNet			Robust AlexNet		
	PSNR (dB) $\uparrow$	SSIM $\uparrow$	LPIPS $\downarrow$	PSNR (dB) $\uparrow$	SSIM $\uparrow$	LPIPS $\downarrow$
1 ( $224 \times 224$ )	15.057	0.3067	0.5473	17.2273	0.3580	0.5665
2 ( $448 \times 448$ )	16.2777	0.4068	0.4234	20.3554	0.4859	0.469
3 ( $672 \times 672$ )	16.0668	0.4317	0.4143	21.3696	0.5265	0.4376
4 ( $896 \times 896$ )	15.4258	0.4655	0.4136	22.575	0.5892	0.4012
5 ( $1120 \times 1120$ )	14.9726	0.4753	0.4235	22.9861	0.6074	0.4018
6 ( $1344 \times 1344$ )	14.3093	0.4887	0.4358	23.4824	0.6527	0.383
7 ( $1568 \times 1568$ )	13.8922	0.4852	0.4587	23.5778	0.6588	0.3898
8 ( $1792 \times 1792$ )	13.4781	0.4967	0.4656	23.7604	0.70178	0.3638
9 ( $2016 \times 2016$ )	13.2869	0.4882	0.4834	23.7907	0.6924	0.3906
10 ( $2240 \times 2240$ )	13.1013	0.4969	0.486	23.9566	0.7244	0.3892

Table A1. Reconstructing upscaled images ( $L \in \{1, \dots, 10\}$ ). Upscaled  $224 \times 224$  ImageNet samples are reconstructed from standard and AR AlexNet features, the latter predominantly obtaining higher accuracy.





Figure A2. Reconstructing upscaled images. Upscaled ImageNet samples are inverted from their standard and AR representations. While standard representations (top row) are severely degraded, AR representations (bottom row) show an outstanding accuracy that improves w.r.t. the scaling factor.

## A2. Results for Additional Applications

### A2.1. Anomaly Detection

Full *one-vs-all* novelty detection results for CIFAR-10 and Cats vs. Dogs datasets are shown in Tab. A3. Reconstructions from AR features consistently obtain a higher accuracy than those from standard representations. Nevertheless, when compared against an alternative anomaly detection method such as ADGAN [9], also based on a generative adversarial model, both standard and AR versions of our proposed model obtain better performance. The training and optimization details used in our anomaly detection

experiments are covered in Sec. A3.2.

### A2.2. Style Transfer

Fig. A5 shows additional stylization results obtained via the Universal Style Transfer algorithm using standard and AR AlexNet autoencoders. Qualitatively, the multi-level stylization approach used in our experiments show that AR representations allow a good texture transferring while better preserving the content image structure. Regardless the type of scene being stylized (*e.g.* landscapes, portraits or single objects), aligning AR robust features allows to preserve sharp edges and alleviates the distortions generated by



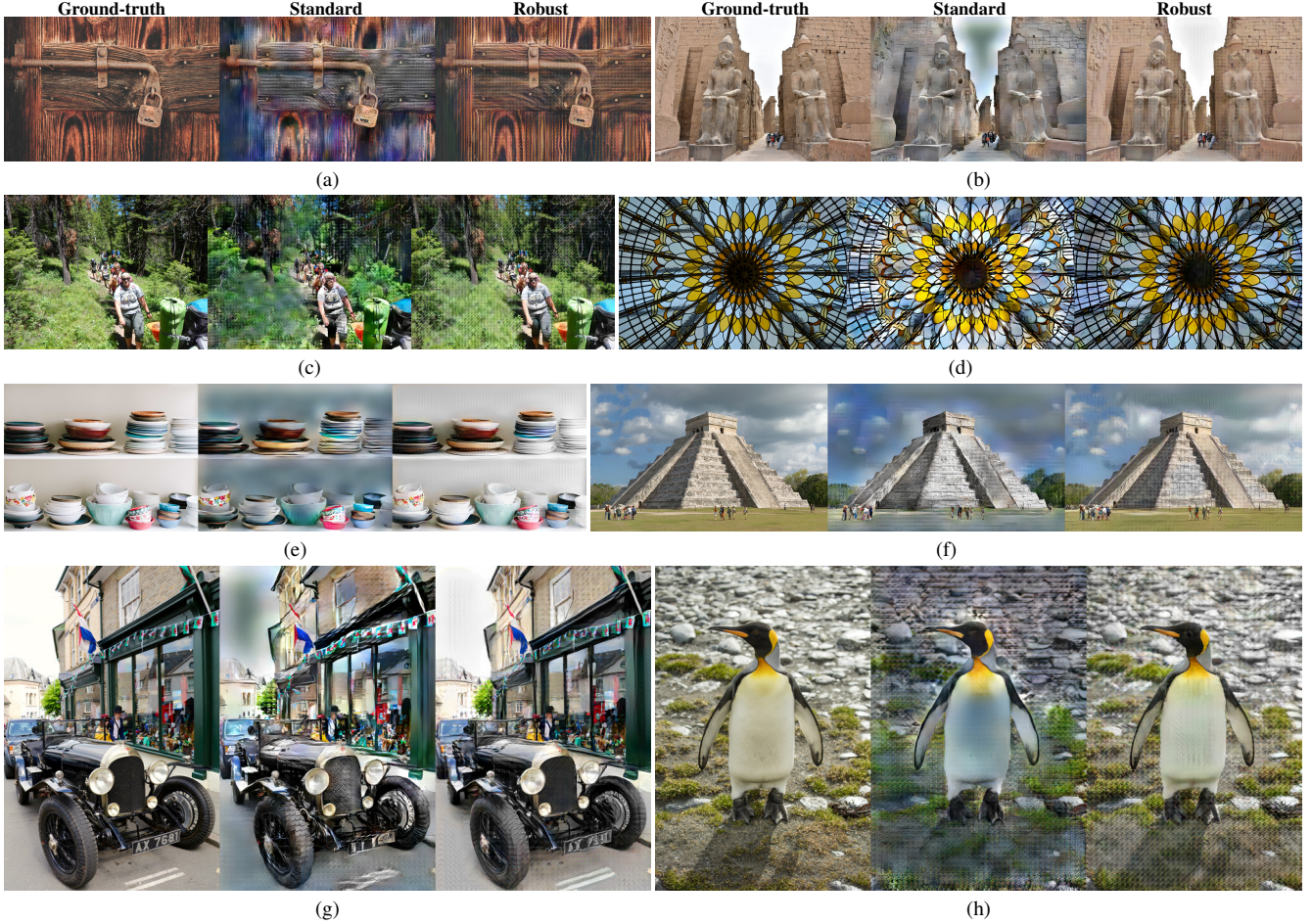


Figure A3. At a resolution of  $2040 \times 1536$ , 10 times higher than the training resolution, standard reconstructions show color and structure degradation. In contrast, reconstructions from our AR autoencoder do not suffer from such distortions and are closer to target DIV2K images.

aligning standard features. Architecture details and training parameters for the style transfer experiments are covered in Sec. A3.3.

### A2.3. Image Denoising

Fig. A6 shows additional denoising results using our standard and AR autoencoders for the CBSDS68, Kodak24 and McMaster sets. As previously discussed, we leverage the low-level feature representations by adding skip connections to our proposed autoencoder. Low-level features complement the contracted feature map obtained from AlexNet conv5, improving the detail preservation. This is observed in the results, both with standard and AR autoencoders.

On the other hand, despite the effect of using skip connections, reconstructions from AR representations show a notorious improvement with respect to standard reconstructions. Specifically, by combining skip connections with the rich information already encapsulated in robust representa-

tions, results on all three datasets show a substantial denoising improvement.

## A3. Implementation Details

### A3.1. Architecture and Training Details

**Encoder.** For all experiments and downstream tasks, the adversarially robust AlexNet classifier was trained using the PGD strategy [34]. The process was performed on ImageNet using stochastic gradient descent. The AR training parameters are as follows:

- Perturbation constraint:  $\ell_2$  ball with  $\varepsilon = 3$
- PGD attack steps: 7
- Step size: 0.5
- Training epochs: 90



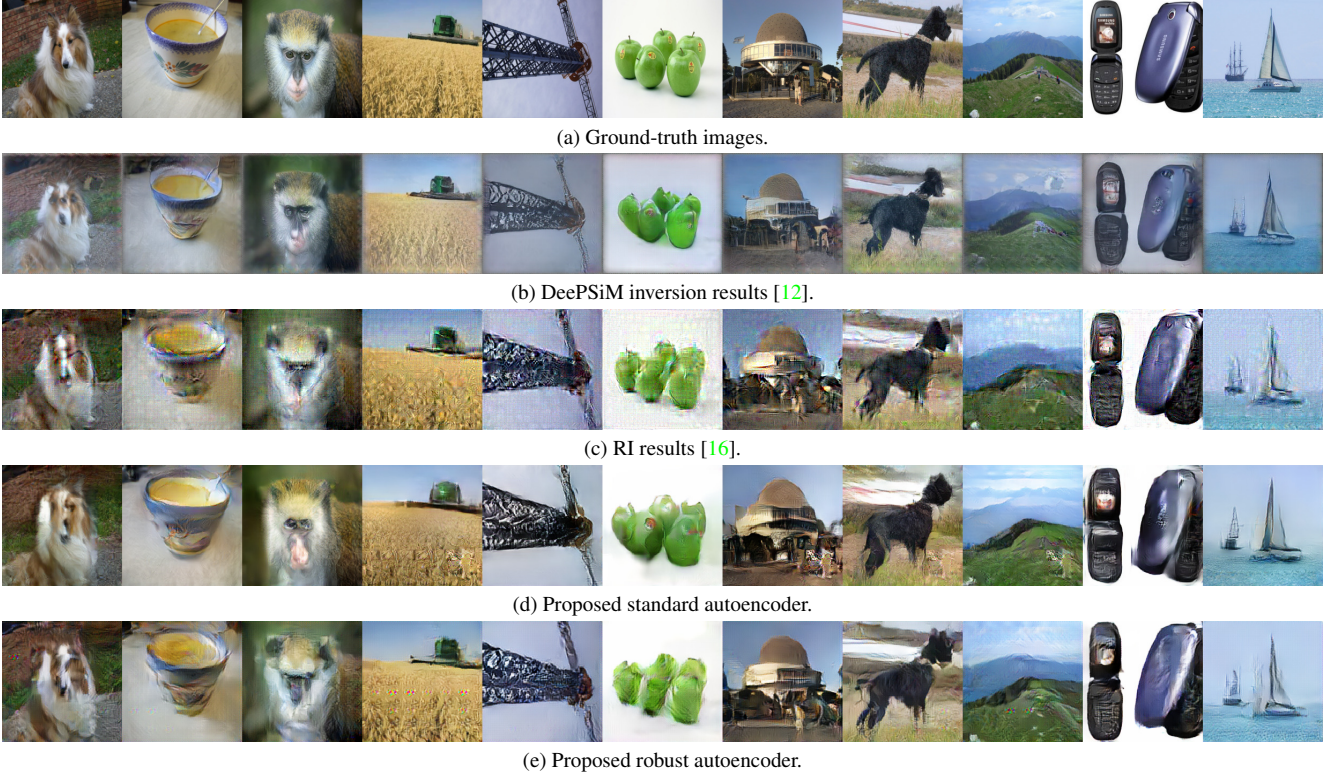


Figure A4. Feature inversion accuracy contrast between our proposed model and alternative inversion methods.

On the other hand, the standard AlexNet classifier was trained using cross-entropy loss as optimization criteria. For both cases, the training parameters were the following:

- Initial learning rate: 0.1
- Optimizer: Learn rate divided by a factor of 10 every 30 epochs.
- Batch size: 256

Tested under AutoAttack ( $\ell_2, \varepsilon = 3$ ), our AR AlexNet obtains a 18.7% top-1 robust accuracy, while our standard AlexNet classifier obtains a 0% top-1 robust accuracy.

AR training was performed using the *Robustness* library [15], based on Pytorch-only code and ran on four Tesla V100 GPUs. Additional details about the model architecture and training parameters used for each experiment and downstream task are as follows.

**Feature Inversion Experiments.** A fully convolutional architecture is used for the decoder or image generator. Tab. A4 describes the decoder architecture used to invert both standard and AR representations, where `conv2d` denotes a 2D convolutional layer, `tconv2d` a 2D transposed convolutional layer, BN batch normalization, ReLU the rectified linear unit operator and `tanh` the hyperbolic tangent operator.

Tab. A5 shows the discriminator architecture, where `leakyReLU` corresponds to the leaky rectified linear unit, `linear` to a fully-connected layer, `apooling` to average pooling and `sigmoid` to the Sigmoid operator. Motivated by the architecture proposed by Dosovitskiy & Brox [12], the discriminator takes as input both a real or fake image and its target conv5 feature map to compute the probability of the sample being real. Fig. A7 shows the discriminator architecture.

Standard and AR autoencoders were trained on ImageNet using  $\ell_1$  per-pixel, perceptual and GAN losses using ADAM. In both cases, all convolutional and transposed convolutional layers are regularized using spectral normalization [38]. Training was performed using Pytorch-only code on two Tesla V100 GPUs. The loss weights and training setup for both standard and AR cases correspond to:

- Generator weights:  $\lambda_{\text{pix}} = 2 \times 10^{-6}$ ,  $\lambda_{\text{feat}} = 1 \times 10^{-2}$ ,  $\lambda_{\text{GAN}} = 100$
- Discriminator weight:  $\lambda_{\text{disc}} = 2 \times 10^{-6}$
- Training epochs: 90
- Generator initial learning rate:  $3 \times 10^{-4}$  (divided by a factor of 10 every 30 epochs).
- Discriminator initial learning rate:  $12 \times 10^{-4}$  (divided by a factor of 10 every 30 epochs).





Figure A5. Style transfer results using standard and robust AlexNet representations. Stylization obtained using the universal style transfer algorithm [32].

- LeakyReLU factor: 0.2
- ADAM  $\beta \in [0, 0.9]$
- Batch size: 128

### A3.2. Anomaly Detection

Standard and AR encoders are fully-trained on ImageNet using the training parameters described in Sec. A1. By freezing the encoder weights, generators are fully-trained using  $\ell_1$  per-pixel and perceptual losses on the dataset of interest, CIFAR10 or Cats vs. Dogs. Input images are

rescaled to  $224 \times 224$  px. before being fed to the model. No data augmentation is applied during the generator training. The regularization parameters for both standard and AR autoencoders were heuristically selected as follows:

- Standard AE:  $\lambda_{\text{pix}} = 2 \times 10^{-3}$ ,  $\lambda_{\text{feat}} = 1 \times 10^{-2}$ .
- Robust AE:  $\lambda_{\text{pix}} = 2 \times 10^{-6}$ ,  $\lambda_{\text{feat}} = 1 \times 10^{-2}$ .

**Optimization in the latent space.** After training the generator on a particular class of interest, the optimal latent code  $\hat{f}$  associated to an arbitrary target image  $x$  is obtained via stochastic gradient descent. For both standard and AR





Figure A6. Image denoising results using standard and AR encoders (AlexNet) from the CBSD68 and Kodak24 sets. Samples corrupted by additive white Gaussian noise ( $\sigma = 50$ ).

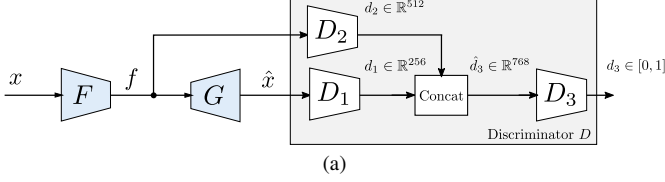


Figure A7. Discriminator model.

autoencoders, the optimization criteria are identical to that used during the generator training. Specifically, we fine-tune  $\hat{f}$  by minimizing the  $\ell_1$  per-pixel and perceptual losses using the following weights:

- Standard AE:  $\alpha_{\text{pix}} = 2 \times 10^{-3}$ ,  $\alpha_{\text{feat}} = 2 \times 10^{-2}$ .
- Robust AE:  $\alpha_{\text{pix}} = 2 \times 10^{-6}$ ,  $\alpha_{\text{feat}} = 2 \times 10^{-2}$ .

The Initial latent code  $\hat{f}^{(0)} \in \mathbb{R}^{6 \times 6 \times 256}$  is drawn from a standard normal distribution and optimized for  $i_{\text{max}} = 100$  iterations. The initial learn rate is chosen as 0.1 and linearly decreases along iterations down to 0.001.

### A3.3. Style Transfer

While, for standard and AR scenarios, the autoencoder associated to conv5 corresponds to the model described in Sec. A3.1, those associated to conv1 and conv2 use Nearest neighbor interpolation instead of transposed convolution layers to improve the reconstruction accuracy and to avoid the checkerboard effect generated by transposed convolutional layers. Tab. A6, and Tab. A7 describe their architecture details.

All generators were fully-trained on ImageNet using Pytorch-only code on two Tesla V100 GPUs. The regularization parameters and training setup for both cases are as follows:

- Standard generator weights:  $\lambda_{\text{pix}} = 2 \times 10^{-4}$ ,  $\lambda_{\text{feat}} = 1 \times 10^{-2}$ .
- AR generator weights:  $\lambda_{\text{pix}} = 2 \times 10^{-6}$ ,  $\lambda_{\text{feat}} = 1 \times 10^{-2}$ .
- Training epochs: 90.
- Generator initial learning rate:  $3 \times 10^{-4}$  (divided by a factor of 10 every 30 epochs).
- ADAM  $\beta \in [0, 0.9]$ .
- Batch size: 128.

### A3.4. Image Denoising

Our image denoising model consists of standard and AR autoencoders equipped with skip connections to better preserve image details. Fig. A8 illustrates the proposed denoising model, where skip connections follow the Wavelet Pooling approach [60]. Tab. A8 and Tab. A9 include additional encoder and decoder architecture details, respectively.

Encoder pooling layers are replaced by Haar wavelet analysis operators, generating an approximation component, denoted as  $\{w_{k,\text{LL}}\}$ , and three detail components, denoted as  $\{w_{k,\text{LH}}, w_{k,\text{HL}}, w_{k,\text{HH}}\}$ , where  $k$  corresponds to the pooling level. While the approximation (low-frequency) component is passed to the next encoding layer, details are skip-connected to their corresponding stages in the decoder. Following this, transposed convolutional layers in the decoder are replaced by unpooling layers (Haar wavelet synthesis operators), reconstructing a signal with well-preserved details at each level and improving the image reconstruction.

In contrast to the AlexNet architecture, all convolutional layers on the decoder use kernels of size  $3 \times 3$ . Also, given the striding factor of the first two AlexNet convolutional layers, two additional interpolation layers of striding factor 2 are used to recover the original input size ( $224 \times 224$ ).

Standard and AR robust generators were trained using exclusively  $\ell_1$  per-pixel and perceptual losses. Training was performed on ImageNet using Pytorch-only code on four Tesla V100 GPUs. Generator loss weights and training parameters for both cases correspond to:

- Generator weights:  $\lambda_{\text{pix}} = 2 \times 10^{-6}$ ,  $\lambda_{\text{feat}} = 1 \times 10^{-2}$ .
- Training epochs: 90.
- Generator initial learning rate:  $3 \times 10^{-4}$  (divided by a factor of 10 every 30 epochs).
- ADAM  $\beta \in [0, 0.9]$ .
- Batch size: 128.

a

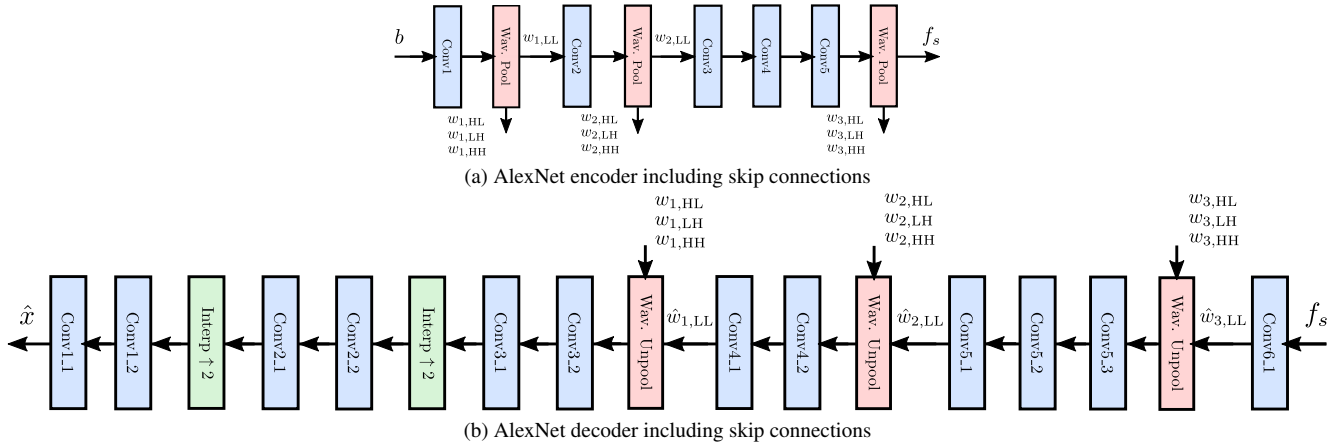


Figure A8. Proposed denoising autoencoder including skip connections.

	$\ell_2$ PGD Attack ( $\epsilon$ )							
	0	0.5	1	1.5	2	2.5	3	3.5
Standard Accuracy	94.93	88.28	81.07	72.47	64.48	64.17	56.77	53.8
$\ell_2$ PGD Attack	28.29	68.75	52.24	41.29	34.45	29.63	25.58	23.48
	( $\epsilon = 0.25$ )	( $\epsilon = 0.5$ )	( $\epsilon = 1.0$ )	( $\epsilon = 1.5$ )	( $\epsilon = 2.0$ )	( $\epsilon = 2.5$ )	( $\epsilon = 3.0$ )	( $\epsilon = 3.5$ )
PSNR (dB) $\uparrow$	14.7259	18.5161	19.2427	<b>19.6278</b>	19.5234	18.7568	19.3713	19.4376
SSIM $\uparrow$	0.2958	0.5179	<b>0.5399</b>	0.5332	0.5265	0.4878	0.501	0.4951
LPIPS $\downarrow$	0.6305	0.5024	<b>0.4832</b>	0.4905	0.5019	0.5312	0.5172	0.5321

Table A2. Reconstruction vs. Robustness. ResNet-18 experiments on CIFAR-10 show that learning to invert contracted features with different AR levels significantly affects the reconstruction accuracy.

Dataset	Positives	ADGAN [9]	Proposed (Standard)	Proposed (Robust)
CIFAR10	0	0.649	<b>0.6874</b>	0.6533
	1	<b>0.39</b>	0.3498	0.3755
	2	0.652	<b>0.6756</b>	0.662
	3	0.481	0.5708	<b>0.6123</b>
	4	0.735	0.751	<b>0.7538</b>
	5	0.476	0.5101	<b>0.5278</b>
	6	0.623	0.6895	<b>0.7113</b>
	7	<b>0.487</b>	0.4773	0.4526
	8	0.66	<b>0.7232</b>	0.7008
	9	0.378	0.362	<b>0.4408</b>
	Average	0.553	0.5797	<b>0.589</b>
Cats vs. Dogs	0	<b>0.663</b>	0.481	0.649
	1	0.481	0.392	<b>0.427</b>
	Average	0.494	0.527	<b>0.538</b>

Table A3. AUROC of our proposed anomaly detection method for each class. Detection evaluated for one-versus-all classification on CIFAR10 and Cats vs. Dogs. Best results highlighted in black.



Layer	Layer Type	Kernel Size	Bias	Stride	Pad	Input Size	Output Size	Input Channels	Output Channels
1a	conv2d + BN + ReLU	$3 \times 3$	✗	1	1	$6 \times 6$	$6 \times 6$	256	256
2a	tconv2d + BN + ReLU	$4 \times 4$	✗	1	1	$6 \times 6$	$7 \times 7$	256	256
2b	conv2d + BN + ReLU	$3 \times 3$	✗	1	1	$7 \times 7$	$7 \times 7$	256	256
3a	tconv2d + BN + ReLU	$4 \times 4$	✗	2	1	$7 \times 7$	$14 \times 14$	256	256
3b	conv2d + BN + ReLU	$3 \times 3$	✗	1	1	$14 \times 14$	$14 \times 14$	256	256
4a	tconv2d + BN + ReLU	$4 \times 4$	✗	2	1	$14 \times 14$	$28 \times 28$	256	256
4b	conv2d + BN + ReLU	$3 \times 3$	✗	1	1	$28 \times 28$	$28 \times 28$	256	128
5a	tconv2d + BN + ReLU	$4 \times 4$	✗	2	1	$28 \times 28$	$56 \times 56$	128	128
5b	conv2d + BN + ReLU	$3 \times 3$	✗	1	1	$56 \times 56$	$56 \times 56$	128	64
6a	tconv2d + BN + ReLU	$4 \times 4$	✗	2	1	$56 \times 56$	$112 \times 112$	64	64
6b	conv2d + BN + ReLU	$3 \times 3$	✗	1	1	$112 \times 112$	$112 \times 112$	64	32
7a	tconv2d + BN + ReLU	$4 \times 4$	✗	2	1	$112 \times 112$	$224 \times 224$	32	32
7b	conv2d + BN + ReLU	$3 \times 3$	✗	1	1	$224 \times 224$	$224 \times 224$	32	3
7c	conv2d + tanh	$3 \times 3$	✓	1	1	$224 \times 224$	$224 \times 224$	3	3

Table A4. Generator architecture used for feature inversion.

Layer	Layer Type	Kernel Size	Bias	Stride	Pad	Input Size	Output Size	Input Channels	Output Channels
Feature Extractor 1 ( $D_1$ )									
1a	conv2d + ReLU	$3 \times 3$	✓	4	1	$256 \times 256$	$56 \times 56$	3	32
2a	conv2d + ReLU	$5 \times 5$	✓	1	1	$56 \times 56$	$52 \times 52$	32	64
2b	conv2d + ReLU	$3 \times 3$	✓	2	1	$52 \times 52$	$23 \times 23$	64	128
3a	conv2d + ReLU	$3 \times 3$	✓	1	1	$23 \times 23$	$21 \times 21$	128	256
3b	conv2d + ReLU	$3 \times 3$	✓	2	1	$21 \times 21$	$11 \times 11$	256	256
4	ave. pooling	$11 \times 11$	—	—	—	$11 \times 11$	$1 \times 1$	256	256
Classifier 1 ( $D_2$ )									
4a	Linear + ReLU	—	✓	—	1	9216	1024	—	—
4b	Linear + ReLU	—	✓	—	1	1024	512	—	—
Classifier 2 ( $D_3$ )									
5a	Linear + ReLU	—	✓	—	1	768	512	—	—
5b	Linear + Sigmoid	—	✓	—	1	512	1	—	—

Table A5. Discriminator architecture used for feature inversion.

Layer	Layer Type	Kernel Size	Bias	Stride	Pad	Input Size	Output Size	Input Channels	Output Channels
1a	conv2d + BN + ReLU	$3 \times 3$	✗	1	1	$27 \times 27$	$27 \times 27$	64	64
2a	tconv2d + BN + ReLU	$4 \times 4$	✗	1	1	$27 \times 27$	$28 \times 28$	64	64
2b	conv2d + BN + ReLU	$3 \times 3$	✗	1	1	$28 \times 28$	$28 \times 28$	64	64
3a	NN interpolation	—	—	2	—	$28 \times 28$	$56 \times 56$	64	64
3b	conv2d + BN + ReLU	$3 \times 3$	✗	1	1	$56 \times 56$	$56 \times 56$	64	64
3c	conv2d + BN + ReLU	$3 \times 3$	✗	1	1	$56 \times 56$	$56 \times 56$	64	32
4a	NN interpolation	—	—	2	—	$56 \times 56$	$112 \times 112$	32	32
4b	conv2d + BN + ReLU	$3 \times 3$	✗	1	1	$112 \times 112$	$112 \times 112$	32	32
5a	NN interpolation	—	—	2	—	$112 \times 112$	$224 \times 224$	32	32
5b	conv2d + BN + ReLU	$3 \times 3$	✗	1	1	$224 \times 224$	$224 \times 224$	32	16
5c	conv2d + BN + ReLU	$3 \times 3$	✗	1	1	$224 \times 224$	$224 \times 224$	16	3
5d	conv2d + tanh	$3 \times 3$	✓	1	1	$224 \times 224$	$224 \times 224$	3	3

Table A6. Conv1 generator architecture used for style transfer.

Layer	Layer Type	Kernel Size	Bias	Stride	Pad	Input Size	Output Size	Input Channels	Output Channels
1a	conv2d + BN + ReLU	$3 \times 3$	✗	1	1	$13 \times 13$	$13 \times 13$	192	192
2a	tconv2d + BN + ReLU	$4 \times 4$	✗	1	1	$13 \times 13$	$14 \times 14$	192	192
2b	conv2d + BN + ReLU	$3 \times 3$	✗	1	1	$14 \times 14$	$14 \times 14$	192	96
3a	NN interpolation	—	—	2	—	$14 \times 14$	$28 \times 28$	96	96
3b	conv2d + BN + ReLU	$3 \times 3$	✗	1	1	$28 \times 28$	$28 \times 28$	96	96
3c	conv2d + BN + ReLU	$3 \times 3$	✗	1	1	$28 \times 28$	$28 \times 28$	96	64
4a	NN interpolation	—	—	2	—	$28 \times 28$	$56 \times 56$	64	64
4b	conv2d + BN + ReLU	$3 \times 3$	✗	1	1	$56 \times 56$	$56 \times 56$	64	64
5a	NN interpolation	—	—	2	—	$56 \times 56$	$112 \times 112$	64	64
5b	conv2d + BN + ReLU	$3 \times 3$	✗	1	1	$112 \times 112$	$112 \times 112$	64	64
6a	NN interpolation	—	—	2	—	$112 \times 112$	$224 \times 224$	64	64
6b	conv2d + BN + ReLU	$3 \times 3$	✗	1	1	$224 \times 224$	$224 \times 224$	64	32
6c	conv2d + BN + ReLU	$3 \times 3$	✗	1	1	$224 \times 224$	$224 \times 224$	32	3
6d	conv2d + tanh	$3 \times 3$	✓	1	1	$224 \times 224$	$224 \times 224$	3	3

Table A7. Conv2 generator architecture used for style transfer.

Layer	Layer Type	Kernel Size	Bias	Stride	Pad	Input Size	Output Size	Input Channels	Output Channels
1a	conv2d + ReLU	$11 \times 11$	✓	4	2	$224 \times 224$	$55 \times 55$	3	64
2a	Wavelet pooling	—	—	2	—	$55 \times 55$	$27 \times 27$	64	64
2b	conv2d + ReLU	$5 \times 5$	✓	1	2	$27 \times 27$	$27 \times 27$	64	192
3a	Wavelet pooling	—	—	2	—	$27 \times 27$	$13 \times 13$	192	192
3b	conv2d + ReLU	$3 \times 3$	✓	1	1	$13 \times 13$	$13 \times 13$	192	384
3c	conv2d + ReLU	$3 \times 3$	✓	1	1	$13 \times 13$	$13 \times 13$	384	256
3c	conv2d + ReLU	$3 \times 3$	✓	1	1	$13 \times 13$	$13 \times 13$	256	256
4a	Wavelet pooling	—	—	2	—	$13 \times 13$	$6 \times 6$	256	256

Table A8. Encoder architecture used for image denoising.

	Layer Type	Kernel Size	Bias	Stride	Pad	Input Size	Output Size	Input Channels	Output Channels
1a	conv2d + BN + ReLU	$3 \times 3$	$\times$	1	1	$6 \times 6$	$6 \times 6$	256	256
2a	Wavelet unpooling	—	—	2	—	$6 \times 6$	$12 \times 12$	256	256
2b	conv2d + BN + ReLU	$3 \times 3$	$\times$	1	1	$12 \times 12$	$12 \times 12$	256	256
2c	Reflection padding	—	—	—	—	$12 \times 12$	$13 \times 13$	256	256
2d	conv2d + BN + ReLU	$3 \times 3$	$\times$	1	1	$13 \times 13$	$13 \times 13$	256	256
2e	conv2d + BN + ReLU	$3 \times 3$	$\times$	1	1	$13 \times 13$	$13 \times 13$	256	192
3a	Wavelet unpooling	—	—	2	—	$13 \times 13$	$26 \times 26$	192	192
3b	Reflection padding	—	—	—	—	$26 \times 26$	$27 \times 27$	192	192
3c	conv2d + BN + ReLU	$3 \times 3$	$\times$	1	1	$27 \times 27$	$27 \times 27$	192	128
3d	conv2d + BN + ReLU	$3 \times 3$	$\times$	1	1	$27 \times 27$	$27 \times 27$	128	64
4a	Wavelet unpooling	—	—	2	—	$27 \times 27$	$55 \times 55$	64	64
4b	Reflection padding	—	—	—	—	$55 \times 55$	$56 \times 56$	64	64
4c	conv2d + BN + ReLU	$3 \times 3$	$\times$	1	1	$56 \times 56$	$56 \times 56$	64	64
5a	NN interpolation	—	—	2	—	$56 \times 56$	$112 \times 112$	64	64
5b	conv2d + BN + ReLU	$3 \times 3$	$\times$	1	1	$112 \times 112$	$112 \times 112$	64	32
5c	conv2d + BN + ReLU	$3 \times 3$	$\times$	1	1	$112 \times 112$	$112 \times 112$	32	32
6a	NN interpolation	—	—	2	—	$112 \times 112$	$224 \times 224$	32	32
6b	conv2d + BN + ReLU	$3 \times 3$	$\times$	1	1	$224 \times 224$	$224 \times 224$	32	3
6c	conv2d + BN + ReLU	$3 \times 3$	$\times$	1	1	$224 \times 224$	$224 \times 224$	3	3
6d	conv2d + tanh	$3 \times 3$	$\checkmark$	1	1	$224 \times 224$	$224 \times 224$	3	3

Table A9. Decoder architecture used for image denoising.